AIAA JOURNAL
Vol. 48, No. 4, April 2010

Fluid–Structure–Acoustics Interaction of the Flow Past a Thin Flexible Structure

Frank Schäfer,* Stefan Müller,† Thomas Uffinger,† Stefan Becker,‡ and Jens Grabinger§
University of Erlangen–Nuremberg, 91058 Erlangen, Germany
and
Manfred Kaltenbacher¶
Alps–Adriadic University, 9020 Klagenfurt, Austria

DOI: 10.2514/1.40344

The acoustic field resulting from the interaction of a thin flexible structure with a turbulent flow was investigated both numerically and experimentally. Two different model configurations were considered: in one a flexible plate acted as a moving wall in a turbulent boundary layer, and in the other the flexible plate was located in the wake of a square cylinder. The fully coupled simulation of the fluid–structure–acoustics interaction was based on a partitioned approach employing two different simulation codes: a finite-volume flow solver of second-order accuracy in space and time and a finite-element structural-mechanics and acoustics solver. A code coupling interface was used for the exchange of data between the different discretizations. The experiments were performed in an acoustic wind tunnel employing microphone measurements of the sound pressure level. Detailed flow measurements were carried out using laser Doppler anemometry and three-component hot-wire anemometry. The flow-induced vibration of the flexible structure was measured with a laser-scanning vibrometer. Experimental and numerical results characterizing the flow field, the structural vibration, and the generated sound are presented.

Nomenclature

CFD	=	Computational fluid dynamics
D	=	Edge length of square cylinder
E	=	Modulus of elasticity
HWA	=	Hot-wire anemometry
LDA	=	Laser Doppler anemometry
LES	=	Large-eddy simulation
Ma	=	Mach number
Re	=	Reynolds number
SPL	=	Sound pressure level
T_{ij}	=	Lighthill's tensor
U	=	Mean velocity in x direction
U_∞	=	Freestream velocity
u_i	=	Unsteady fluid velocity
$\overline{u'u'}$, $\overline{v'v'}$	=	Components of the Reynolds stress tensor
V	=	Mean velocity in y direction
y^+	=	Nondimensional wall scale
β, γ	=	Parameters in the Newmark time discretization
ρ_0	=	Mean density
ρ_s	=	Density of mechanical structure

I. Introduction

IN MANY technical applications, the flow of a fluid past a flexible platelike structure leads to structural vibrations and thereby to the generation of vibrational sound. Coverings and panelings of cars and airplanes are important examples of this kind of fluid–structure–acoustics interaction. Usually, the sound generated by the flow-induced vibrations is considered as noise, and its reduction is a topic of major interest.

The emission of noise due to flow-induced vibrations of a flexible plate has received much attention in the literature. Many of the efforts are related to applications in aviation and automotive engineering. One of the early investigations in this direction was the work of Davies [1], in which the excitation of a thin flexible panel by wall-pressure fluctuations of a turbulent boundary layer was studied using modal analysis. The boundary-layer excitation of flexible plates and the resulting emission of noise have also been investigated by, e.g., Graham [2], Howe and Shah [3], Frampton and Clark [4], and Mazzoni and Kristiansen [5]. In most of the studies, the influence of the fluid on the flexible plate is modeled based on spectra of the turbulent wall-pressure fluctuations in the boundary layer. The flow above the plate is not resolved in detail. A more explicit treatment of the flow over the plate was performed by Zolotarev [6] and Tang et al. [7], who modeled the fluid flow using potential theory. Tang et al. [7] estimated the sound resulting from the interaction between a single model vortex and a flexible wall in order to investigate the basic mechanisms of the fluid–structure–acoustics interaction. With respect to the treatment of the fluid flow, studies considering a highly resolved flow based on the Navier–Stokes equations are rare. There is also very little work toward a fully coupled treatment of fluid flow, structural mechanics, and acoustics at a realistic level of detail (see, e.g., Vergne et al. [8]). However, such a methodology would be very helpful for improving our understanding of the mechanisms leading to the emission of sound and for taking measures toward a reduction in vibrational noise.

In the present work, the interaction of a fluid flow with a thin flexible structure and the resulting acoustic field were studied in detail. For this purpose, a test case was developed for both experimental and numerical investigations, which represents a simplified model of a car underbody. A description of the test case is given in the following section. A fully coupled computation scheme was applied for the simulation of the complex interaction between fluid, structure, and acoustics. The scheme is based on a partitioned approach employing a finite-volume flow solver and a finite-element structural-mechanics and acoustics solver. A code coupling interface is used for the exchange of data between the finite-volume and the finite-element discretization. An important feature of the computational scheme is that it allows for a separate prediction of

Presented as Paper 3058 at the 14th AIAA/CEAS Aeroacoustics Conference, Vancouver, Canada, 5–7 May 2008; received 10 August 2008; revision received 7 December 2009; accepted for publication 3 January 2010. Copyright © 2010 by Stefan Becker. Published by the American Institute of Aeronautics and Astronautics, Inc., with permission. Copies of this paper may be made for personal or internal use, on condition that the copier pay the $10.00 per-copy fee to the Copyright Clearance Center, Inc., 222 Rosewood Drive, Danvers, MA 01923; include the code 0001-1452/10 and $10.00 in correspondence with the CCC.

*Research Scientist, Institute of Fluid Mechanics.
†Ph.D. Student, Institute of Process Technology and Systems Engineering.
‡Senior Scientist, Institute of Process Technology and Systems Engineering. Member AIAA.
§Ph.D. Student, Department of Sensor Technology.
¶Professor for Applied Mechatronics. Member AIAA.

flow-induced and vibrational sound. The experiments were mainly performed in a low-noise wind tunnel using microphone measurements, laser Doppler anemometry (LDA) and three-component hot-wire anemometry (HWA). Flow-induced structural vibrations were measured with a laser-scanning vibrometer. Further details of the numerical and the experimental methods are given below. Finally, the results of the study concerning the flow field, the vibration of the flexible plate, and the generated sound are presented.

II. Test Case

The investigation was based on a simplified geometric model, which is nevertheless complex enough to represent all important features of relevant technical application cases. The basic setup consisted of a flexible platelike structure, which is part of an otherwise rigid wall (Fig. 1). To study the influence of geometric flow disturbances on the resulting acoustic field, two different configurations were investigated: one case with a square-cylinder obstacle in front of the flexible plate as shown in Fig. 1a and the other without an obstacle (Fig. 1b). In the remainder of the paper, the two configurations are referred to as case A and case B, respectively.

The plate was made of stainless steel with a thickness of 40 μm. The density was $\rho_s = 7850$ kg/m^3, the modulus of elasticity was $E = 2 \cdot 10^{11}$ kg/ms^2, and Poisson's ratio equalled 0.3. The plate was prestressed in the main flow direction at a value of $7 \cdot 10^6$ N/m^2. In case A, the edge length of the square cylinder was $D = 0.02$ m. The streamwise extension of the flexible plate amounted to $7.5D$ in both configurations. Because of the prestressing, the plate was clamped over a length of $0.5D$ at both the upstream and downstream edges.

A flow of air at ambient conditions was considered. Different freestream velocities U_∞ ranging from 10 to 40 m/s were studied experimentally. In the simulation, the case $U_\infty = 20$ m/s was investigated, corresponding to a Reynolds number of $Re = 26000$ based on U_∞ and D.

III. Numerical Method

A partitioned computation scheme was used for the simulation of the fluid–structure–acoustics interaction of the present test case. A schematic is shown in Fig. 2. Two different simulation codes were employed. The numerical flow computation was carried out with FASTEST-3D [9], a finite-volume CFD solver developed at the Institute of Fluid Mechanics, University of Erlangen–Nuremberg. For the structural mechanics and the acoustics computations, the finite-element multiphysics solver CFS++ [10,11] is applied, which has been developed at the Department of Sensor Technology, University of Erlangen–Nuremberg.

In the present computation scheme, the effect of the acoustics on the structure and the fluid is neglected. This approach is feasible if the expected acoustic pressure fluctuations are much smaller than the overall fluid pressure. Provided that the structure is located in the acoustic near field, where many uncorrelated acoustic sources due to the unsteady flow field are present, the coherence length of the acoustic waves impacting the structure is small, which makes an

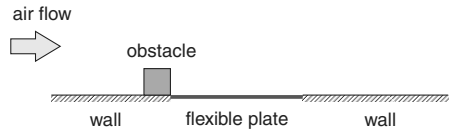

a) Case A

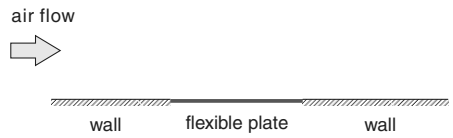

b) Case B

Fig. 1 Setup of the test case.

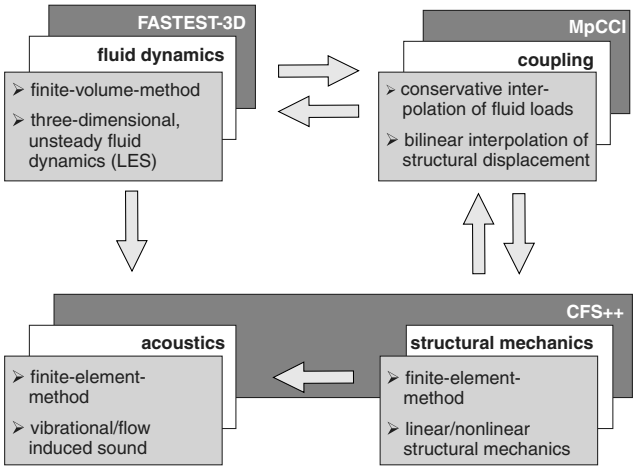

Fig. 2 Coupled computation scheme for the simulation of fluid–structure–acoustics interactions.

excitation of eigenmodes of the structure due to acoustics implausible. Both preconditions were fulfilled for the test cases presented in this work. Therefore, the feedback of acoustics on the fluid and on the structure could be neglected. Based on this simplification, the fluid–structure–acoustics interaction was split into three parts, which were treated independently: fluid–structure interaction, fluid–acoustics coupling, and structure–acoustics coupling. A detailed description of the resulting computation scheme was given by Ali et al. [12], Kaltenbacher et al. [13], and Schäfer et al. [14,15]. For fluid–structure interaction, an implicit, strong coupling between FASTEST-3D and CFS++ is applied. Accordingly, the two solvers iterate within each time step until a dynamic equilibrium between fluid field and structural displacement is reached (in the present investigation, two iterations per time step were sufficient). This leads to a more stable computational scheme than in the case of an explicit coupling, in which only one iteration per time step is performed. In each iteration, the fluid mesh is adapted to the new position of the structure by applying fast interpolation methods, which typically need less than 0.5% of the total computation time. For small structural deformations, which were considered in the present work, cell quality is preserved by this simple mesh-adaptation procedure. The exchange of data between the finite-volume and the finite-element discretization is realized by MpCCI [16]. The acoustics computations are performed with CFS++ using a finite-element discretization of the wave equation, which describes the propagation of sound to the far field. Structure–acoustics coupling is achieved in CFS++ by applying appropriate boundary conditions to the wave equation [15]. The computation of flow-induced noise (fluid–acoustics coupling) is based on Lighthill's [17,18] analogy. Details of the modeling can be found elsewhere [13].

The flow simulation was carried out by solving the incompressible Navier–Stokes equations with discretizations of second-order accuracy in both space and time. The flow domain considered in case A is depicted in Fig. 3a. Basically, the same setup was used in case B, but without obstacle. For all walls, no-slip boundary conditions were chosen, whereas, for the upper face, a symmetry boundary condition was used. In the spanwise direction, periodic boundary conditions were employed. At the inflow, the streamwise velocity was set according to measured data resembling a laminar profile with $U_\infty = 20$ m/s and a boundary-layer thickness of 3.48 mm. In the experiment, the maximum turbulence level of the profile was found to be below 0.6%. For reasons of simplification, these small temporal fluctuations of the inflow profile are neglected in the simulation. At the outflow, a convective boundary condition was used. With these boundary conditions, in case A it was observed that the laminar boundary layer remained stable until the flow disturbance due to the obstacle led to laminar–turbulent transition. In case B, however, using inflow/outflow boundary conditions it was difficult to obtain a turbulent flow field because of the absence of the square cylinder. For this reason, in case B periodic boundary conditions were used in the

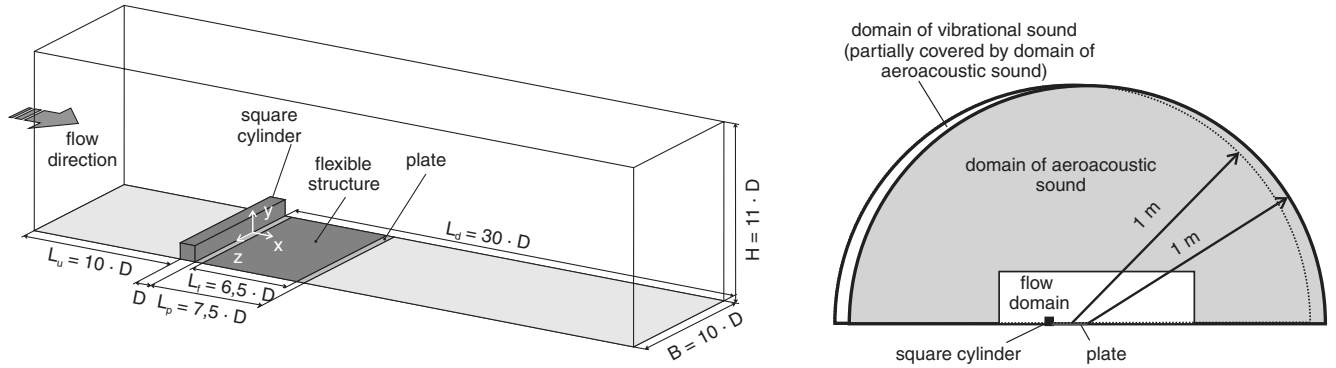

a) Flow domain **b) Acoustics domains**

Fig. 3 Computational domains.

streamwise direction together with an initial disturbance of the boundary layer, and the streamwise pressure gradient was chosen to yield the same freestream velocity U_∞ as in the experiment. In both cases A and B, the temporal development of the flow field was computed until a fully developed turbulent state was reached, before fluid–structure interaction was initiated.

Turbulence was modeled by performing large-eddy simulations (LES) based on the Smagorinsky model with the Smagorinsky constant set to a value of 0.1. For time discretization, an implicit three-point scheme of second-order accuracy was employed. Since all boundary layers have to be resolved properly, block-structured meshes with up to 8 million control volumes were used for the spatial discretization of the flow domain. The mesh density was higher at the walls and decreased toward the other boundaries. The dimensionless wall scale y^+ of the first grid point next to the wall did not exceed a value of 0.4 based on the time-averaged velocity field. In the spanwise direction, an equidistant grid with 48 control volumes was used.

For structural mechanics, we solved the equations for linear elasticity by applying the finite-element method. The flexible plate was discretized using 13,000 hexahedral elements with bilinear finite-element basis functions. To avoid the well-known shear locking occurring in thin structures such as ours, we applied the incompatible mode approach [19,20]. Since the computations are performed in time domain, we used the Newmark scheme for the time discretization [21]. Using values of 0.25 and 0.5 for the two time-discretization parameters β and γ we achieve a second-order absolute stability scheme. A modal damping of the vibrating structure could be introduced by using Rayleigh's damping model [21], in which the numerical damping matrix is computed out of the weighted sum of the mass and stiffness matrix. The weighting factors would then be calculated from the modal damping factor (loss factor), which can be experimentally obtained [21]. However, in all our computations no mechanical damping was applied to the vibrating structure. Furthermore, we have used standard mechanical material values for the stainless steel plate (density ρ_s of 7850 $\mathrm{kg/m^3}$, modulus of elasticity E of $2.0 \cdot 10^{11}$ $\mathrm{N/m^2}$, and Poisson's ratio of 0.3) and adjusted the prestressing to meet the first measured eigenfrequency of 140 Hz obtained by a hammer test.

For the acoustic-field computation, we solve once for the vibrational sound and once for the flow-induced sound. In the first case, we use the linear wave equation and apply the finite-element method. The coupling to the mechanical field is obtained by forcing the continuity of the mechanical surface velocity and the acoustic-particle velocity in normal direction at the common interface [10]. In the second case, we solve the variational formulation of Lighthill's inhomogeneous wave equation again by applying the finite-element method. The inhomogeneous part is obtained by the second spatial derivative of Lighthill's tensor T_{ij}, which computes for our case (incompressible flow at low Mach number and isentropic state) as

$$T_{ij} = \rho_0 u_i u_j \tag{1}$$

with the mean density ρ_0 and the flow velocities u_i. In the variational formulation, the second spatial derivative can be reduced to a first-order one [22]. Furthermore, to preserve the acoustic energy, we perform an integration over the source volume (corresponding to the computational flow region) within the finite-element formulation and project the results to the nodes of the fine-flow grid, which has to be interpolated to the coarser acoustics grid (for details we refer to [22]).

For both approaches, vibrational and flow-induced sound, we performed the computations in the time domain. We use Newmark's scheme for the time discretization with the same parameters as in the structural-mechanics simulation. Furthermore, the computational domain of the acoustics computations was larger than the flow domain, since we are interested in the radiation of noise to the far field. A schematic is shown in Fig. 3b. The acoustic domains were centered around the flow domain and the plate, respectively, in order to have the acoustic sources in the center of the domains. Up to 420,000 hexahedral finite elements with bilinear basis functions were used for the spatial discretization of the acoustic domains, which corresponded to up to 20 finite elements per smallest acoustic wavelength. First-order absorbing boundary conditions were applied at the top boundary in order to guarantee free radiation conditions [23].

IV. Experimental Method

The acoustics measurements were performed in the acoustic wind tunnel of the University of Erlangen–Nuremberg, which is equipped with sound absorbers (anechoic chamber condition). A description of the acoustic wind tunnel was given by Hahn et al. [24]. Additional flow measurements were carried out in the wind tunnel of the Institute of Fluid Mechanics.

The general setup of the experiments was almost the same as for the simulation, but additional cases with different geometries and locations of the obstacle in front of the flexible plate were investigated. For this work the configurations corresponding to the numerical setup were chosen. The spanwise extension of the plate was $33D$. The plate was mounted on a massive aluminum construct to avoid coupling between plate and mounting. A sketch of the setup is depicted in Fig. 4.

The velocity field of the flow was measured using LDA. To avoid contamination of the aeroacoustic wind-tunnel absorbers due to the particle seeding necessary in the LDA measurement technique, this part of the experiment was carried out in a classical aerodynamic wind tunnel. The LDA measurement technique allowed reliable measurements in the recirculation region behind the obstacle and in the flow field close to the vibrating surface of the flexible plate. The LDA system employed was specially designed for application in low-speed wind tunnels [25]. Because of high turbulence intensities in the region behind the square cylinder, statistical analysis indicated that approximately 20,000 measurements are necessary at each location to obtain statistically valid results. This corresponded to a maximum measurement time of about 120 s at each location. Following the statistical procedure outlined by Bendat and Piersol [26], for a 95% confidence interval the statistical uncertainty is 0.8%

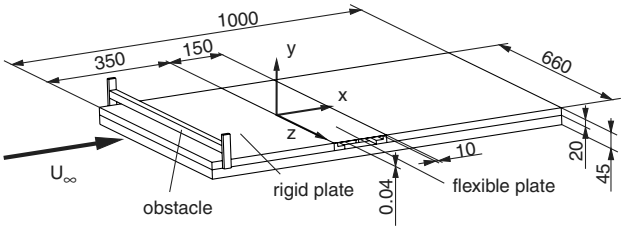

Fig. 4 Schematic drawing of the experimental setup.

in the case of the mean velocity and 1.3% in the case of root mean square quantities. In the outer flow with lower turbulence intensities, the uncertainty is less than 0.01%.

For the measurement of turbulent velocity fluctuations at high sample rates, HWA using a three-component hot-wire probe (Dantec StreamLine System) was applied. At each location, a measurement time of 55 s was used at a sample rate of 20 kHz.

A microphone at a 1 m distance perpendicular to the plate was used for the sound measurements. Phase-resolved measurements with a scanning vibrometer were carried out to identify the vibration modes of the flexible plate. For this purpose, a single-point Polytec vibrometer was used together with a scanning vibrometer to observe the flexural modes of the plate at different frequencies. The single-point vibrometer constantly detected the vibrations of one point on the plate while the surface of the plate was scanned with the scanning vibrometer. To investigate the structure–acoustics interaction, correlation measurements with the scanning vibrometer and the microphone were performed.

Phase-resolved LDA measurements were made by coupling the LDA system with the single-point vibrometer, which acquired the plate vibration. The setup in the wind-tunnel is depicted in Fig. 5. The vibrometer signal was monitored with a tracker expecting the first eigenfrequency and dynamically detecting the modulation of the frequency in a range of ± 30 Hz. The current frequency was transmitted to the LDA system, in which the incoming signals were matched with the period length, so allowing for a time-dependent visualization of the flow field at a certain frequency.

V. Results

As stated in Sec. II, this paper concentrates on the cases depicted in Fig. 1. The freestream velocity U_∞ of the approaching flow was 20 m/s, unless specified otherwise.

A. Flexible Plate with Square Cylinder (Case A)

1. *Flow Field*

The normalized average velocity field obtained by LDA measurements and simulation is depicted in Fig. 6a. The most prominent flow structure is a large region of recirculation that is located behind the square cylinder. Qualitatively, we found a good overall agreement between simulation and experiment. There is a difference of only 11% in the recirculation length, which is shorter in the experiments. In the simulation, higher velocity values in the main flow above the recirculation region can be observed than in the experiment. This can be attributed to the symmetry boundary condition used in the simulation at the top boundary of the domain. Although the top boundary was chosen to be far away from the square cylinder, the symmetry condition still causes a channel effect, which overemphasizes the acceleration of the fluid above the recirculation.

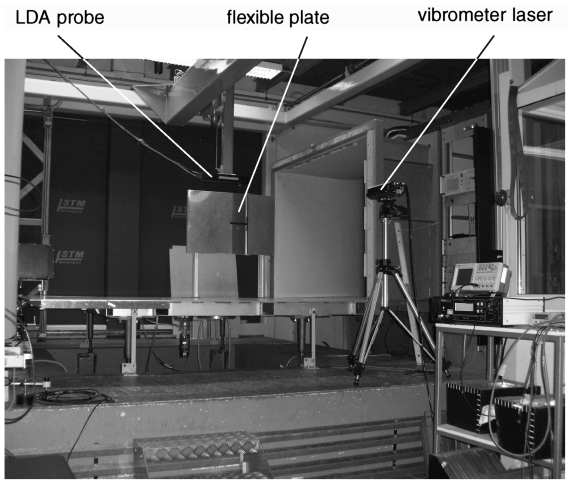

Fig. 5 Setup of the phase-resolved LDA measurements.

The distribution of the measured and the computed turbulent kinetic energy normalized to the maximum achieved value is shown in Fig. 6b. Both in experiment and simulation, turbulence develops in the shear layer between the main flow and the region of flow separation. However, there is a remarkable difference that in the experiment the onset of turbulence is earlier than in the simulation. In particular, in the measurements there is already some turbulent energy in front of the square cylinder, which is not the case in the computation. This means that the flow in front of the obstacle is already transitional in the experiment, whereas, in the simulation, transition to turbulence is initiated in the shear layer above the square cylinder and the recirculation bubble. The transition process in the simulation can be seen from Fig. 7. Here, a shear layer instability causes the approaching laminar flow to become turbulent. The reason for the later transition in the computation is possibly the applied inflow velocity profile. Although the profile is in accordance with measured data resembling a laminar profile, there are minor temporal fluctuations in the measurement that are not included in the computation. In particular, the earlier onset of turbulence in the experiment contributes to the observed shortening of the recirculation region due to increased turbulent momentum transport in the vertical direction. Moreover, the overacceleration of the flow due to the upper symmetry boundary might also contribute to the longer recirculation length in the simulation.

The above findings are supported by comparisons of vertical profiles based on numerical and experimental data shown in Fig. 8. Two different positions above the flexible plate are chosen, one at a short distance ($1D$) behind the square cylinder (Fig. 8a) and another one in the middle of the plate ($4D$ behind the cylinder, Fig. 8b). For each position, the time-averaged and normalized velocities in x and y direction and the two normalized components $\overline{u'u'}$ and $\overline{v'v'}$ of the Reynolds stress tensor are compared. The normalization is based on the freestream velocity and the maximum values of $\overline{u'u'}$ and $\overline{v'v'}$, respectively, in the whole flow field. The figures confirm the issues mentioned above. In the simulation the symmetry boundary condition at the top side of the numerical flow domain leads to an overacceleration of the fluid above the region of recirculation. Furthermore, the high values of $\overline{u'u'}$ and $\overline{v'v'}$ are moved further downstream in the simulation due to the later transition compared with the experimental data.

2. *Fluid–Structure Interaction*

The computed displacements of the flexible plate due to fluid–structure interaction are shown in Fig. 9. Figure 9a depicts the temporal evolution of the deformation at a point in the center of the flexible plate. Before $t = 0$, the flow is computed without fluid–structure interaction in order to obtain a fully developed turbulent flow over the square cylinder. At $t = 0$, the plate is made flexible and fluid–structure interaction is initiated. As can be seen, the plate starts to oscillate with an average displacement in the upwards direction, which is due to the local pressure minimum located in the recirculation region behind the square cylinder. Below the plate ambient pressure is assumed. The frequency of the oscillation is about 140 Hz, which is in very good agreement with the first eigenfrequency of the plate at 142 Hz, obtained by an eigenfrequency analysis. Frequency spectra of the plate deformation and the plate velocity are shown in Fig. 9b. In addition to the first eigenfrequency, higher oscillation modes can also be seen, which correspond to the

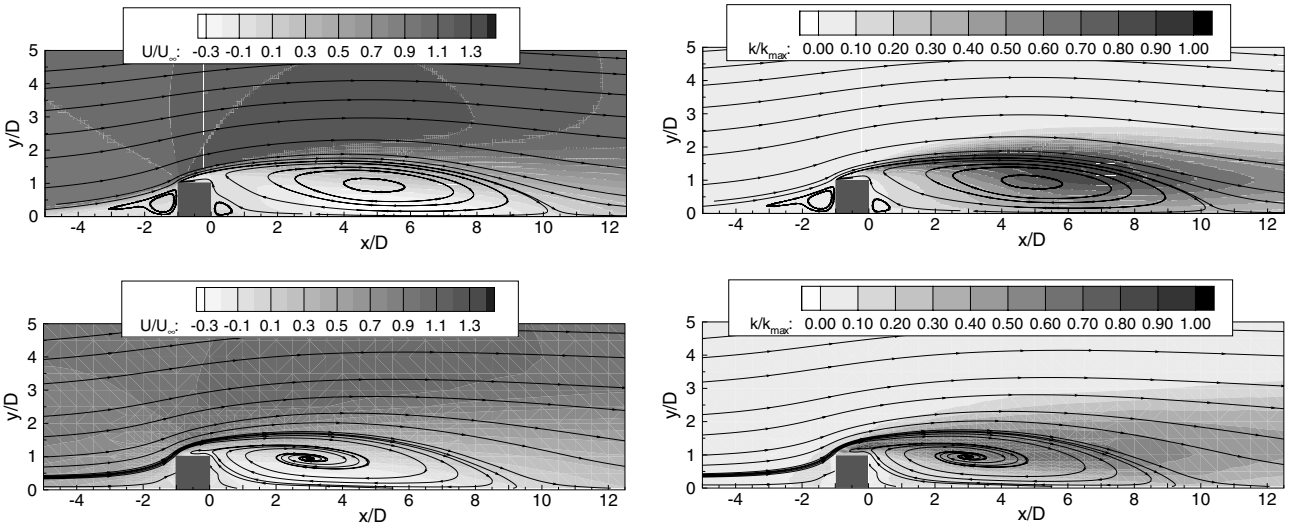

a) Average velocity in main flow direction: simulation (top) and experiment (bottom)

b) Distribution of turbulent kinetic energy: simulation (top) and experiment (bottom)

Fig. 6 Comparison of measured and computed average flow field (case A).

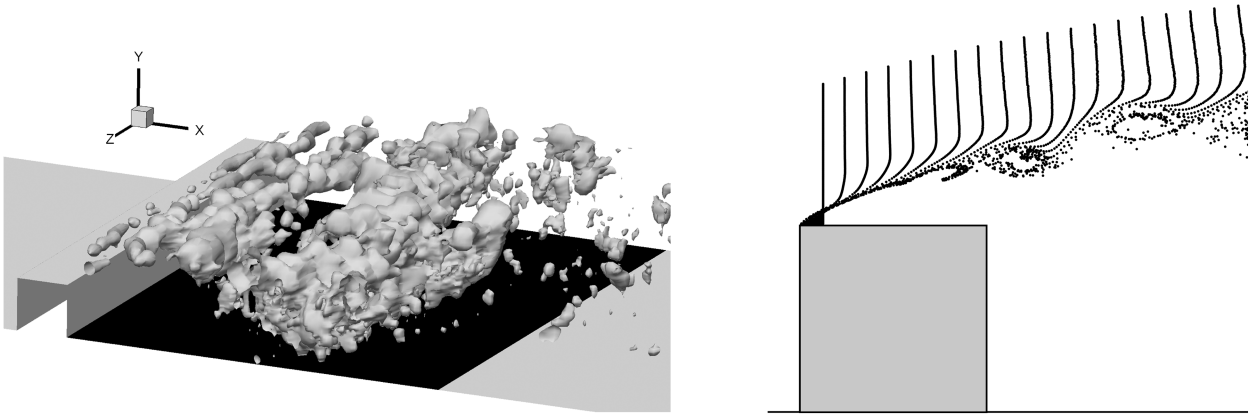

a) Isosurfaces of pressure at an arbitrary instant of time

b) Timeline visualization at an arbitrary instant of time

Fig. 7 Vortex shedding in the unstable shear layer between the main flow and the region of flow separation.

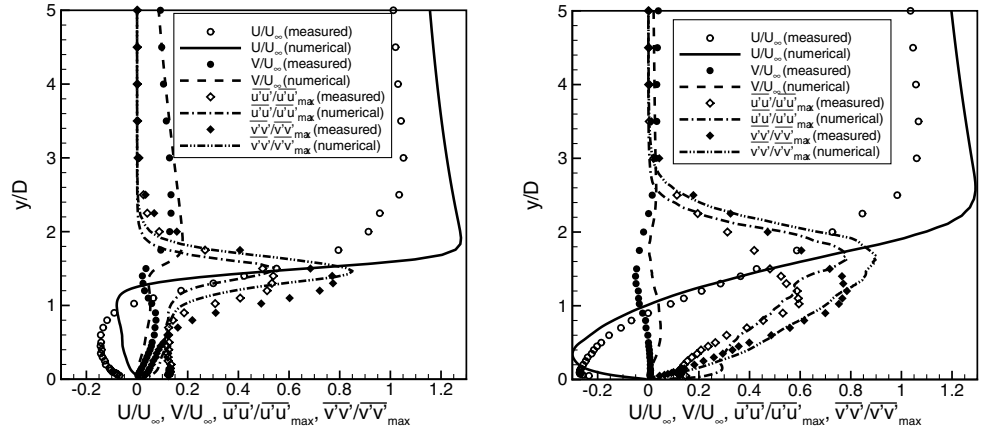

a) At a distance *D* behind the square cylinder

b) At a distance 4 *D* behind the square cylinder

Fig. 8 Comparison of vertical profiles based on numerical and experimental data: normalized velocity components in *x* and *y* direction and two normalized components of the Reynolds stress tensor.

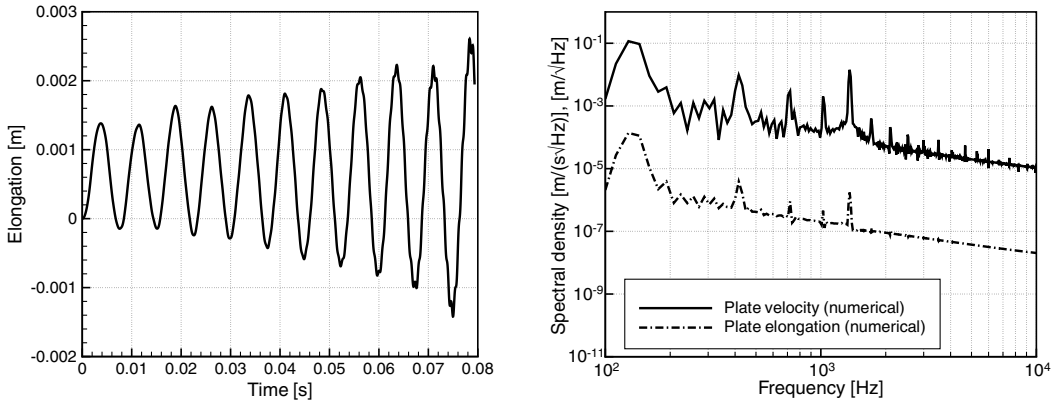

a) Deformation at a point in the center of the plate

b) Frequency spectra of the deformation and the velocity of a point in the center of the plate

Fig. 9 Computed displacement of the flexible plate (case A).

odd eigenfrequencies of the flexible plate as obtained by the eigenfrequency analysis (see Table 1).

It has to be noted that the mechanical displacement of the displayed point in Fig. 9a shows an increasing amplitude with time, caused by the mechanical computations, which did not take into account any damping. This argumentation is supported by simple numerical simulation of the plate excited by a time-varying pressure load with a frequency near the first eigenfrequency. The time-domain computation also resulted in a vibrating plate with increasing amplitude similar to the one displayed in Fig. 9a for the fully coupled fluid–structural computations. Furthermore, modes beyond the first eigenfrequency were not observed in the experiments. This indicates that the damping of the experimental setup is significant and should be taken into account for further investigations.

The bending of the plate at an arbitrary instant of time is visualized in Fig. 10. It can be seen that the displacement is clearly dominated by the first eigenmode. A higher-order mode with smaller amplitude is also visible. The deformation is homogeneous in the spanwise direction. Although the plate has a large number of nonhomogeneous eigenmodes, none of these is observed in the present simulation.

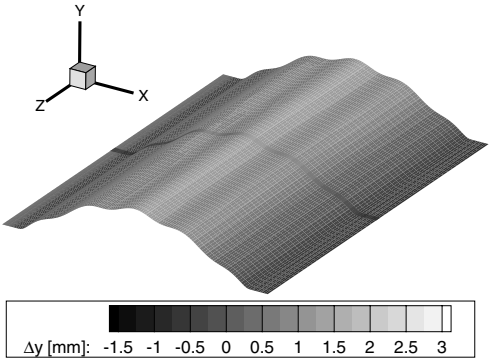

Fig. 10 Snapshot of the computed plate displacement at an arbitrary instant of time (case A, displacement magnified by a factor of 20).

3. Acoustic Results

Frequency spectra of the measured sound pressure level are plotted in Fig. 11a. Spectra obtained for the empty test section, for the flexible plate without obstacle (case B) and for the flexible plate with square cylinder (case A), are provided. The discussion in this section concentrates on case A (for case B, see Sec. V.B). In comparison with the empty test section, the sound radiation of the flexible plate with obstacle shows a prominent peak at about 140 Hz, which is very close to the first numerical eigenfrequency at 142 Hz. Additionally, at higher frequencies a large increase in broadband noise is observed. The tonal peak between 500 and 600 Hz is not relevant since it is also present in the measurement of the empty test section. The results of the vibrometer measurements indicate that the first low-frequency peak is due to the structural vibration of the flexible plate, whereas the high-frequency broadband noise is due to flow-induced sound (compare Sec. V.B.1, Fig. 17). This is also supported by measurements of the correlation between the sound pressure at the microphone position and the velocity of the vibrating plate. The corresponding coherence spectrum is shown in Fig. 11b. A strong correlation is found between 100 and 200 Hz, which is in good agreement with the spectrum of the sound pressure level in Fig. 11a. Apart from this, there is a smaller peak in the coherence spectrum between 500 and 600 Hz that corresponds to a peak in the sound pressure spectrum, which is already present in the empty test section. This indicates that there is an influence from the wind tunnel or the test rig causing a vibration of the plate in the frequency range from 500 to 600 Hz.

In the simulation, the flow-induced sound and the vibrational sound were calculated separately. The resulting flow-induced sound based on the Lighthill analogy is shown in Fig. 12 for three different angular positions on the boundary of the acoustical computational domain (see Fig. 3b). An angle of 0° corresponds to the mean flow direction. The frequency spectra of the sound pressure level in Fig. 12a exhibit a broadband character with an elevation between 100 and 200 Hz. In the phase of the simulation before starting the fluid–structure interaction, this elevation cannot be found. It seems that there is a minor influence of the plate vibration on the flow-induced sound. The directivity pattern in Fig. 12b is comparable to a dipole with a neutral axis varying between 60 and 90°, where angle zero corresponds to the main flow direction. However, at some frequencies significant deviations from the dipole characteristics can be observed. Again, the picture is different in the phase of the simulation before starting the fluid–structure interaction, in which a dipole directivity with a neutral axis at 60° is constantly found over a wide frequency range.

Table 1 First ten computed eigenfrequencies of the plate in Hz (same boundary conditions applied as used for the coupled fluid–structural computations)

1st	2nd	3rd	4th	5th	6th	7th	8th	9th	10th
142.2	168.3	229.6	285.3	300.0	306.4	340.5	390.5	399.7	430.18

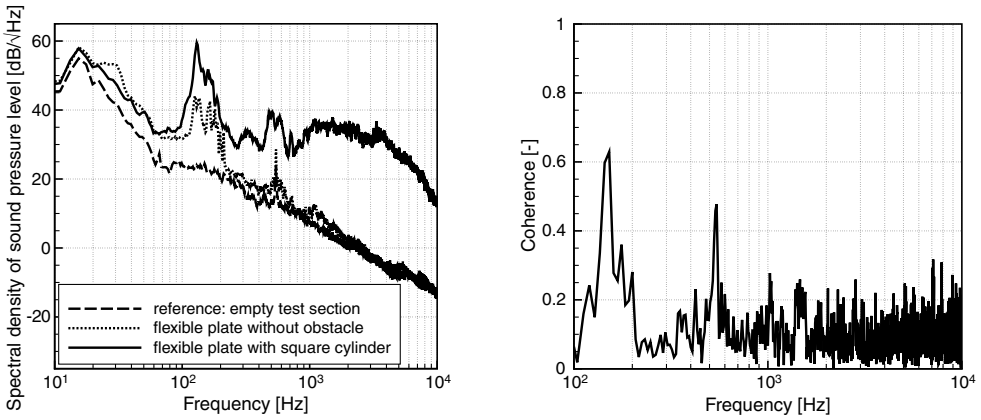

a) Sound pressure level at a 1 m distance perpendicular to the plate (cases A and B)

b) Coherence spectrum (case A)

Fig. 11 Spectra of the measured sound pressure level and of the coherence between sound pressure signal and plate velocity signal.

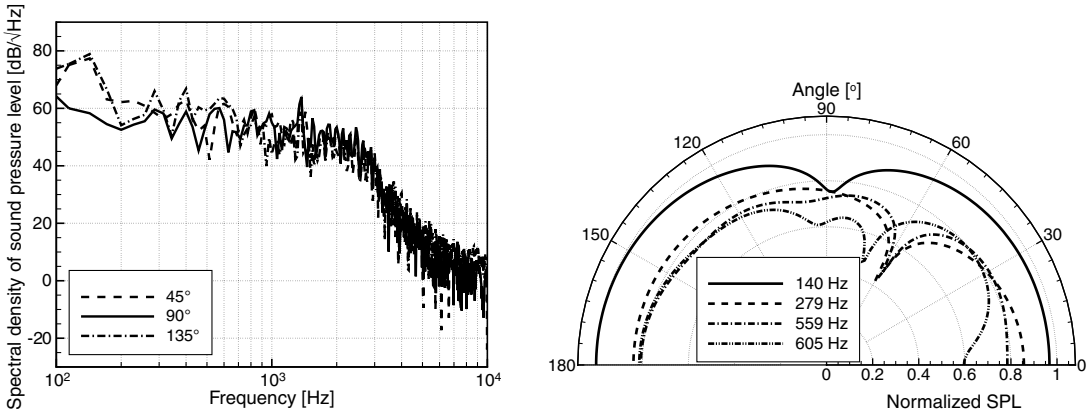

a) Frequency spectra at 45, 90, and 135°

b) Directivity pattern at different frequencies

Fig. 12 Computed flow-induced sound at a distance of 1 m from the downstream edge of the plate (case A).

Frequency spectra of the computed vibrational sound pressure level are plotted in Fig. 13. A prominent peak can be found next to the first eigenfrequency of the plate, together with several higher-frequency peaks corresponding to the higher oscillation modes of the plate. This is in good accordance with the spectra of the plate oscillation presented in Fig. 9b.

The computed and measured spectra of the total sound pressure level at a distance of 1 m perpendicular to the center of the plate are compared in Fig. 14. The total sound based on the numerical computations can be calculated by adding the squared sound pressures of the spectra of the flow-induced and the vibrational sound. Compared with the experimental data, the measured tonal component between 100 and 200 Hz agrees well with the first peak found in the simulation. However, as for all tonal components in the spectra due to vibrational sound, the computed sound pressure level is significantly higher at the peaks than the measured values, whereas between the peaks the computed and the measured levels are of the same order of magnitude. The high peak values of the computed sound pressure can be attributed to the increasing amplitude of the simulated plate oscillation shown in Fig. 9a. Increasing amplitude at the same frequency leads to increasing plate velocity and thereby to higher sound pressure values. As already mentioned in Sec. V.A.2, the increasing oscillation amplitudes is a consequence of neglecting the damping in the mechanical computation. We expect that the differences between the measured and simulated sound pressure levels will be strongly reduced by applying an appropriate damping model within the numerical simulation of the mechanical field. The level of the flow-induced sound is noticeably higher in the simulation than in the experiment. The reason for the high sound pressure levels of the numerical method was not fully investigated so far and will be a matter for future work.

B. Flexible Plate Without Obstacle (Case B)

1. Fluid–Structure Interaction

The computed displacements of the flexible plate without the square cylinder are shown in Fig. 15. Qualitatively, the results are very similar to those obtained for case A (compare Fig. 9), but significant quantitative differences can be found. Most importantly,

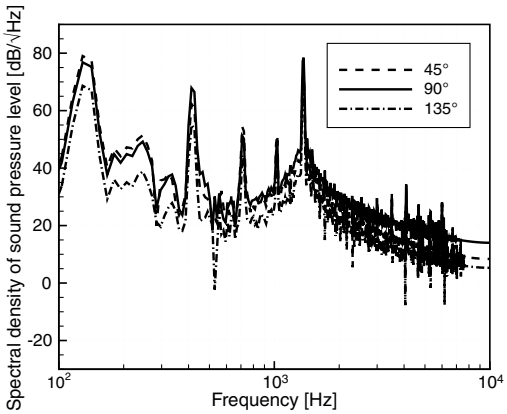

Fig. 13 Computed vibrational sound at a distance of 1 m from the center of the plate (case A).

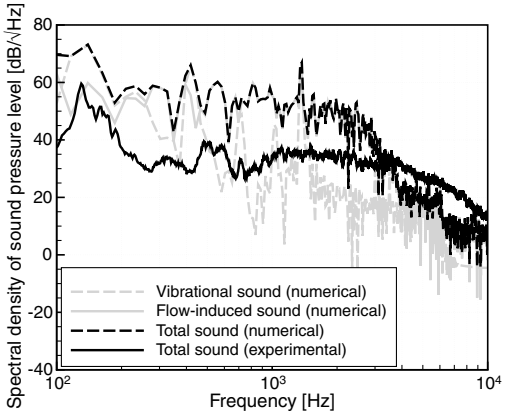

Fig. 14 Comparison of computed and measured spectra of the sound pressure level in a distance of 1 m perpendicular to the center of the flexible plate.

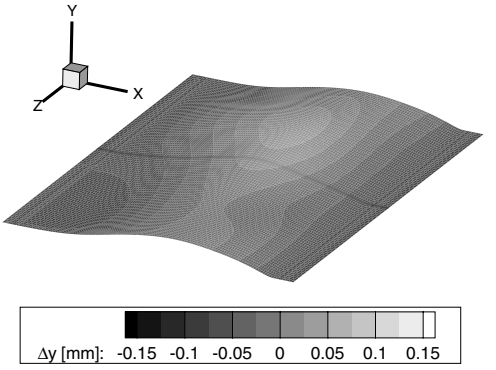

Fig. 16 Snapshot of the computed plate displacement at an arbitrary instant of time (case B, displacement magnified by a factor of 50).

without an obstacle the amplitudes of the oscillation are a factor of about 10 smaller than with the square cylinder. The same was observed for the computed fluid load on the plate. This indicates that the excitation of the plate by the turbulent boundary layer in case B is much weaker than that by the flow in the wake of the square cylinder in case A.

Frequency spectra of the plate deformation and the plate velocity are plotted in Fig. 15b. Compared with case A, the frequency of the most dominant mode is shifted toward 120 Hz, which is significantly less than the first eigenfrequency of the plate at 142 Hz. The same applies to the observed higher-frequency modes, which do not coincide with the odd eigenfrequencies of the plate but can be related to other, partly nonhomogeneous eigenmodes. The inhomogeneity of the plate oscillation is revealed by Fig. 16, which shows the bending of the plate at an arbitrary instant of time. Whereas in case A the plate deformation was always homogeneous in the spanwise direction, in case B this homogeneity is lost.

Results of the vibrometer measurements are shown in Fig. 17. Frequency spectra of the measured vibration amplitude of the plate are provided in Fig. 17a for both cases A and B. The spectrum for the setup with obstacle shows major contributions at frequencies between 50 and 190 Hz. Significant peaks are found at 170 and 150 Hz, which roughly correspond to the first numerical eigenfrequency of the plate at 142 Hz. In case B, a significantly smaller vibration amplitude is found than in case A. This is in good qualitative agreement with the numerical results. Although the quantitative values of the vibration amplitude differ between experiment and simulation, the tendency is predicted correctly by the computational method.

2. *Acoustic Results*

Frequency spectra of the measured sound pressure level for case B are plotted in Fig. 11a. The spectrum shows several peaks in the range between 100 and 200 Hz. In the higher-frequency range, there is only a small difference from the reference case with the empty test section.

The sound pressure level of the tonal noise component in Fig. 11a is much lower in the case without the obstacle than in the case with the square cylinder. However, this finding cannot be generalized. In the measurements a strong influence of the freestream velocity U_∞ on the acoustic field was observed. Experimental results for $U_\infty = 40$ m/s are depicted in Fig. 18a. The sound pressure levels are significantly higher than for $U_\infty = 20$ m/s. The difference of 17.65 dB in the total sound pressure level for case A corresponds very well with the value of 18 dB of a Ma^6 law for the acoustic power. A difference of 13.79 dB for case B is close to a Ma^5 dependency.

In case of a freestream velocity of $U_\infty = 40$ m/s, the presence of the obstacle leads to a peak that is lower and wider than without the obstacle. To understand this phenomenon, three-component hot-wire measurements were made in two lines 10 and 20 mm above the plate. Figure 18b shows the measured data plotted in an anisotropy invariant map [27]. In contrast to the case without the obstacle, the case with the obstacle can be found in the lower middle of the invariant map; i.e., the turbulence generated by the obstacle in the region behind the square cylinder is much closer to isotropic turbulence than in the flow field without the obstacle. Since isotropic turbulence is normally located in highly three-dimensional flow fields, the correlation length of turbulent patterns is very short. This leads to an uncorrelated excitation of the plate and consequently to a reduction in the peak of the tonal frequency and to more broadband noise than in the better correlated flow without the obstacle.

The computed flow-induced sound for $U_\infty = 20$ m/s is displayed in Fig. 19. A broadband frequency spectrum can be observed with no

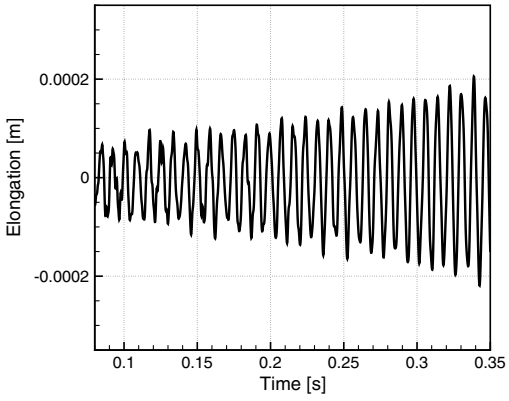

a) Deformation at a point in the center of the plate

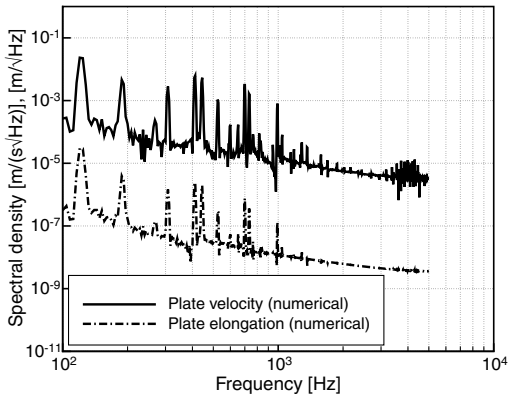

b) Frequency spectra of the deformation and the velocity of a point in the center of the plate

Fig. 15 Computed displacement of the flexible plate (case B).

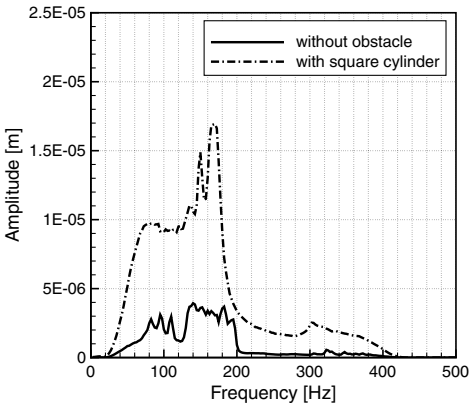

a) Frequency spectra of the measured vibration amplitude, averaged over plate area

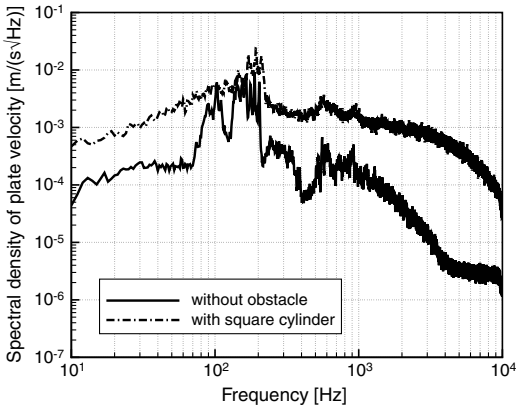

b) Frequency spectra of the measured vibration velocity at the center point of the plate

Fig. 17 Measured vibration amplitude and vibration velocity spectra (cases A and B).

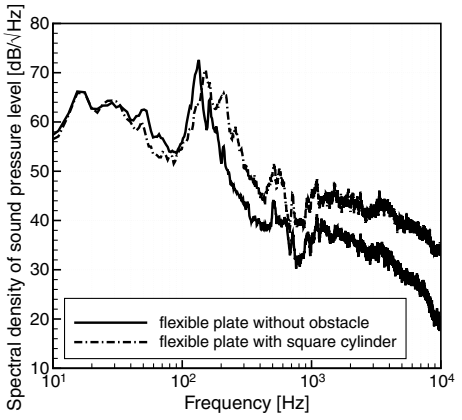

a) Measured sound pressure level

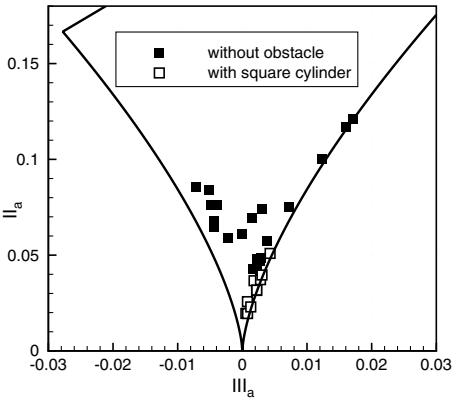

b) Invariant map with three-component hot-wire measurement data

Fig. 18 Experimental results for $U_\infty = 40$ m/s (cases A and B).

significant elevation in the vicinity of the plate's major oscillation frequency. Flow-induced sound and plate vibration seem to be fully decoupled, whereas in case A a slight influence of the plate vibration was found. This might be attributed to the smaller vibration amplitude in case B, which certainly leads to a smaller influence of the vibration on the flow field. Apart from the elevation between 100 and 200 Hz in case A, below 400 Hz the computed sound pressure level is of the same order of magnitude in both cases A and B. Above 400 Hz, a more rapid decrease is seen for the case without the obstacle.

The computed vibrational sound is plotted in Fig. 20. It is found that the amplitudes of the most prominent peaks are significantly lower than in case A. This is in accordance with expectation, since in case B the vibration amplitude of the plate is approximately one order

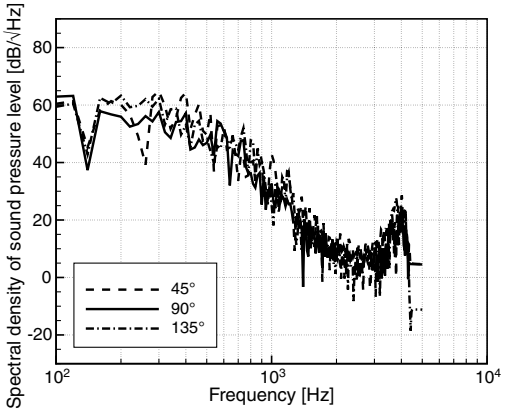

a) Frequency spectra at 45, 90, and 135°

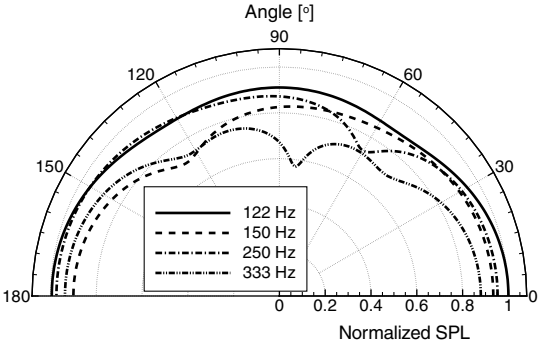

b) Directivity pattern at different frequencies

Fig. 19 Computed flow-induced sound at a distance of 1 m from the downstream edge of the plate (case B).

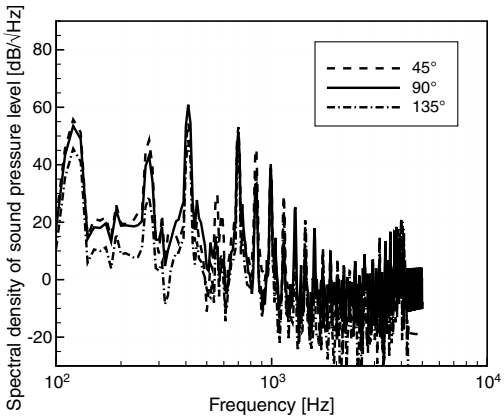

Fig. 20 Computed vibrational sound at a distance of 1 m from the center of the plate (case B).

of magnitude smaller than in case A, whereas the vibration frequency is similar. This leads to a smaller plate velocity and thereby to a reduced acoustic-particle velocity and sound pressure.

VI. Discussion

Comparing the frequency spectra of the computed sound pressure level with the experimental findings in Fig. 14, despite quantitative differences it can be seen that the overall tendency in the experiment is well reflected by the simulations. In both experiment and simulation the flow disturbance caused by the square cylinder leads to a significant increase in sound pressure level compared with the case without the obstacle (at $U_\infty = 20$ m/s). The tonal component observed between 100 and 200 Hz in the measurements corresponds well to the computed vibrational sound due to the first eigenmode of the plate. The rise in tonal noise that was detected in the measurements on switching from case B to case A was also found in the simulation of vibrational sound. The computed flow-induced noise was more intense at high frequencies in the square-cylinder case than in the case without an obstacle. Qualitatively, this is in good accordance with the experiments, in which broadband noise is observed in the high-frequency range in case A whereas it is not present in case B. Hence, the numerical results indicate that the broadband noise is not due to the plate vibration but to the turbulent flow past the square cylinder. This is also supported by the correlation measurements discussed in Sec. V.A.3.

Despite this qualitative agreement, there are major differences between the simulations and the experiments. The higher-order vibration modes of the plate that were found in the simulation were not observed in the experiments. Strong peaks in the numerical simulations resulted from not considering the mechanical damping to the vibrating plate, while, in the measurements, just the fundamental eigenfrequency within the plate structure was found. This clearly indicates that the damping behavior of the experimental setup is significant and has to be taken into account for any numerical simulation. Another discrepancy arose in the computed sound pressure levels, which were significantly higher than the measured values. However, as far as the vibrational sound was concerned, this was only true for the peak values; between the peaks, the computed and the measured levels were of the same order of magnitude. The high peak values of the computed sound pressure indicated that the amplitude of the simulated plate oscillation was too high, again as a consequence of the undamped mechanical simulation model. Future work will be conducted on an appropriate mechanical damping model.

VII. Conclusions

Experimental and numerical investigations on the noise produced by the flow over a thin flexible plate have been presented. Two different configurations were considered: one case with a square-cylinder obstacle located in front of the flexible plate and the other without an obstacle.

A fully coupled computation scheme was used for the simulation of the complex interaction between fluid, structure, and acoustics. The scheme was based on a partitioned approach employing two different simulation codes: a finite-volume flow solver and a finite-element structural-mechanics and acoustics solver. MpCCI was applied for the exchange of data between the two discretizations. The experiments were performed in an acoustic wind tunnel employing microphone measurements, LDA, and three-component HWA. The flow-induced vibration of the flexible structure was measured with a laser-scanning vibrometer.

In the experiments, a strong influence of the freestream velocity U_∞ on the radiated sound field was found. For low freestream velocity ($U_\infty = 20$ m/s), the introduction of the square-cylinder obstacle led to a significant increase in sound pressure level compared with the case without an obstacle. However, at higher velocity ($U_\infty = 40$ m/s), a decrease in the tonal noise component was observed. This was attributed to the stronger isotropy of the turbulent fluctuations in the wake of the square cylinder in comparison to the flow without the obstacle, leading to a less correlated excitation of the flexible plate.

The overall tendency of the computed sound pressure level was in good accord with the tendency found in the experiments, though some quantitative values differed significantly. The computed plate oscillation and the resulting vibrational sound were found to make a major contribution to the first eigenmode of the flexible plate. Additionally, higher-order modes were observed in the simulation. The measured sound pressure level was dominated by the first eigenmode, showing a broad band character at higher frequencies in the square-cylinder case. Since the higher-order modes in the simulation were not found in the measurements, this indicates that the damping behavior of the experimental setup is significant, and an appropriate damping model for the numerical simulation of the plate has to be applied.

Acknowledgments

Financial support from the Bavarian Research Foundation (Bayerische Forschungsstiftung, BFS) and the German Research Foundation (DFG 894) are gratefully acknowledged.

References

[1] Davies, H. G., "Sound from Turbulent-Boundary-Layer-Excited Panels," *Journal of the Acoustical Society of America*, Vol. 49, No. 3, Part 2, 1971, pp. 878–889. doi:10.1121/1.1912428

[2] Graham, W. R., "Boundary Layer Induced Noise in Aircraft, Part 1: The Flat Plate Model," *Journal of Sound and Vibration*, Vol. 192, No. 1, 1996, pp. 101–120. doi:10.1006/jsvi.1996.0178

[3] Howe, M. S., and Shah, P. L., "Influence of Mean Flow on Boundary Layer Generated Interior Noise," *Journal of the Acoustical Society of America*, Vol. 99, No. 6, 1996, pp. 3401–3411. doi:10.1121/1.414988

[4] Frampton, K. D., and Clark, R. L., "Power Flow in an Aeroelastic Plate Backed by a Reverberant Cavity," *Journal of the Acoustical Society of America*, Vol. 102, No. 3, 1997, pp. 1620–1627. doi:10.1121/1.420073

[5] Mazzoni, D., and Kristiansen, U., "Finite Difference Method for the Acoustic Radiation of an Elastic Plate Excited by a Turbulent Boundary Layer: A Spectral Domain Solution," *Flow, Turbulence and Combustion*, Vol. 61, Nos. 1–4, 1998, pp. 133–159. doi:10.1023/A:1026440919022

[6] Zolotarev, I., "Fluid–Structural–Acoustical Interactions of a Thin Plate in a Channel with Flowing Fluid," *American Society of Mechanical Engineers*, Vol. 1, 1997, pp. 403–410.

[7] Tang, S. K., Leung, R. C. K., So, R. M. C., and Lam, K. M., "Acoustic Radiation by Vortex Induced Flexible Wall Vibration," *Journal of the Acoustical Society of America*, Vol. 118, No. 4, 2005, pp. 2182–2189. doi:10.1121/1.2011127

[8] Vergne, S., Auger, J.-M., Périé, F., Jacques, A., and Nicolopoulos, D., "Aeroelastic Noise," *Large-Eddy Simulation for Acoustics*, edited by C. Wagner, T. Hüttl, and P. Sagaut, Cambridge Univ. Press, Cambridge, England, U. K., 2007, pp. 272–293, ISBN 978-0-521-87144-0.

[9] Durst, F., and Schäfer, M., "A Parallel Block-Structured Multigrid Method for the Prediction of Incompressible Flows," *International Journal of Numerical Methods in Fluids*, Vol. 22, No. 6, 1996, pp. 549–565.

[10] Kaltenbacher, M., *Numerical Simulation of Mechatronic Sensors and Actuators*, 2nd ed., Springer–Verlag, Berlin, 2007, ISBN 978-3-540-71359-3.

[11] Kaltenbacher, M., Hauck, A., Triebenbacher, S., Link, G., and Bahr, L., "CFS + +: Coupled Field Simulation," Department of Sensor Technology, University of Erlangen, TR 1-07, Erlangen, Germany, 2007.

[12] Ali, I., Escobar, M., Kaltenbacher, M., and Becker, S., "Time Domain Computation of Flow Induced Sound," *Computers and Fluids*, Vol. 37, No. 4, 2008, pp. 349–359.
doi:10.1016/j.compfluid.2007.02.011

[13] Kaltenbacher, M., Escobar, M., Ali, I., and Becker, S., "Numerical Simulation of Flow-Induced Noise Using LES/SAS and Lighthill's Acoustics Analogy," *International Journal for Numerical Methods in Fluids* [online journal], 2009.
doi: 10.1002/fld.2123

[14] Schäfer, F., Ali, I., Becker, S., Kaltenbacher, M., Escobar, M., and Link, G., "Computational Aeroacoustics using MpCCI as Coupling Interface between Fluid Mechanics, Structural Mechanics and Acoustics," *Proceedings of the 7th MpCCI User Forum*, Institute of Algorithms and Scientific Computing, St. Augustin, Germany, 2006, pp. 98–111.

[15] Schäfer, F., Kniesburges, S., Uffinger, T., Becker, S., Grabinger, J., Link, G., and Kaltenbacher, M., "Numerical Simulation of Fluid–Structure and Fluid–Structure–Acoustic Interaction Based on a Partitioned Coupling Scheme," *High Performance Computing in Science and Engineering, Munich 2007*, Springer–Verlag, Berlin, 2008, pp. 335–348, ISBN 978-3-540-69181-5.

[16] Ahrem, R., Hackenberg, M. G., Redler, R., and Roggenbunck, J., "MpCCI Mesh Based Parallel Code Coupling Interface," Institute of Algorithms and Scientific Computing (SCAI), http://www.mpcci.org.

[17] Lighthill, M. J., "On Sound Generated Aerodynamically: 1. General Theory," *Proceedings of the Royal Society (London) A*, Vol. 211, No. 1107, 1952, pp. 564–587.
doi:10.1098/rspa.1952.0060

[18] Lighthill, M. J., "On Sound Generated Aerodynamically: 2. Turbulence as a Source of Sound," *Proceedings of the Royal Society (London) A*, Vol. 222, No. 1148, 1954, pp. 1–32.
doi:10.1098/rspa.1953.0049

[19] Taylor, R., Beresford, P., and Wilson, E., "A Non-Conforming Element for Stress Analysis," *International Journal for Numerical Methods in Engineering*, Vol. 10, No. 6, 1976, pp. 1211–1219.
doi:10.1002/nme.1620100602

[20] Bischoff, M., and Romero, I., "A Generalization of the Method of Incompatible Modes," *International Journal for Numerical Methods in Engineering*, Vol. 69, No. 9, 2007, pp. 1851–1868.
doi:10.1002/nme.1830

[21] Hughes, T. J., *The Finite Element Method*, Dover, New York, 2000.

[22] Kaltenbacher, M., Escobar, M., Becker, S., and Ali, I., "Computational Aeroacoustics Based on Lighthill's Acoustic Analogy," *Computational Acoustics of Noise Propagation in Fluids*, edited by S. Marburg, and B. Nolte, Chap. 4, Springer–Verlag, Berlin, 2008, pp. 115–142, , ISBN 978-3-540-77447-1.

[23] Engquist, B., and Majda, A., "Absorbing Boundary Conditions for the Numerical Simulation of Waves," *Mathematics of Computation*, Vol. 31, No. 139, 1977, pp. 629–651.
doi:10.2307/2005997

[24] Hahn, C., Becker, S., Ali, I., Escobar, M., and Kaltenbacher, M., "Investigation of Flow Induced Sound Radiated by a Forward Facing Step," *New Results in Numerical and Experimental Fluid Mechanics 6*, edited by C. Tropea, S. Jakirlic, H.-J. Heinemann, R. Henke, and H. Hönlinger, Springer–Verlag, Berlin, 2007, pp. 438–445, ISBN 978-3-540-74458-0.

[25] Becker, S., Lienhart, H., and Durst, F., "Flow Around Three-Dimensional Obstacles in Boundary Layers," *Journal of Wind Engineering and Industrial Aerodynamics*, Vol. 90, Nos. 4–5, 2002, pp. 265–279.
doi:10.1016/S0167-6105(01)00209-4

[26] Bendat, J. S., and Piersol, A. G., *Random Data Analysis and Measurement Procedures*, Wiley, New York, 1986, ISBN 0-471-04000-2.

[27] Lumley, J. L., "Computational Modelling of Turbulent Flows," *Advances in Applied Mechanics*, Vol. 18, 1978, pp. 123–176.
doi:10.1016/S0065-2156(08)70266-7